Mon. Not. R. Astron. Soc. **342,** 383–398 (2003)

Spatial distribution of near-infrared and optical emission properties in the bipolar nebula Menzel 3

Nathan Smith★†

Center for Astrophysics and Space Astronomy, University of Colorado, 389 UCB, Boulder, CO 80309, USA

Accepted 2003 February 4. Received 2003 January 26; in original form 2002 December 16

ABSTRACT

Ground-based optical spectra combined with near-infrared spectra and images of the young bipolar planetary nebula Menzel 3 (Mz 3) reveal positional variations in extinction, excitation, density and other characteristics. Interstellar extinction is probably less than $A_V = 2.65$, while extinction toward the nucleus is approximately 4.6 mag. The lobes show stratified ionization, with high-excitation emission localized at high latitudes. Quantitative analysis using the CLOUDY spectral synthesis code suggests that the polar lobes 'see' an excitation source similar to a blackbody of roughly 36 000 K and 10 000 $L_{\odot}$, and chemical abundances reveal that the ejecta have He enhanced by a factor of ∼2, and N enhanced more strongly, with N/O∼1. The lobes are probably radiatively excited, but shocks may heat the 'blisters' at the polar axis. The bright, unresolved nucleus has a crowded emission spectrum distinct from the diffuse bipolar lobes, and it indicates high electron densities of 10^6–10^7 cm^{-3}. An equatorial disc-like geometry for dense gas in the nucleus is likely. The nucleus also shows a nearly power-law continuum; when corrected for reddening it may require two stars, one hot star and one cool giant, along with hot ∼900-K dust. A distance up to ∼2.5 kpc is possible. In general, the spectral characteristics of Mz 3 are similar to those of the well-studied nebula M 2-9, and the two objects may share a similar evolutionary history. However, an important difference between them is that Mz 3 appears to be mostly devoid of molecular hydrogen, while infrared H_2 lines are conspicuous in M 2-9.

Key words: circumstellar matter – stars: evolution – stars: mass-loss – planetary nebulae: general – planetary nebulae: individual: Mz 3.

1 INTRODUCTION

Menzel 3 (Mz 3; Menzel 1922) is a striking bipolar nebula in the southern hemisphere that is presumably a young planetary nebula. It extends more than 50 arcsec along its major axis, although its two bright polar lobes are ∼12 arcsec in diameter and osculate at a bright, unresolved nucleus (Evans & Thackeray 1950; Evans 1959; Lopez & Meaburn 1983; Redman et al. 2000). Outer filaments extending almost linearly toward the polar directions from the bright rotund lobes, combined with the bright nucleus, evoke an ant-like form to some observers; its complex morphology and unusual spectrum have apparently earned it the distinction of being called the 'Chamber of Horrors' of planetary nebulae (Evans 1959). The ionized polar lobes and splattered outer debris of Mz 3 show interesting line profiles, indicating radial expansion at ∼50 km s^{-1} with the polar axis tilted out of the plane of the sky by approximately 30° (Lopez & Meaburn 1983; Meaburn & Walsh 1985). Faster material has also been seen expanding along the poles (Redman et al. 2000). Cohen et al. (1978) proposed an exciting star with a temperature of ∼32 000 K and spectral type of O9.5 or B0. They also found a distance to Mz 3 of 1.8 kpc, but this remains uncertain (see Lopez & Meaburn 1983). Thermal infrared (IR) images reveal dust in the nebula, but most of the IR flux comes from the bright nucleus (Aitken & Roche 1982; Quinn et al. 1996). Dust resides on thin surfaces of the polar lobes and the limb-brightened edges are polarized, suggesting that they are mostly hollow (Scarrott & Scarrott 1995), reminiscent of the 'Homunculus' around η Carinae (Smith 2002). Obscuring dust may also be concentrated toward the equatorial plane of the system (Cohen et al. 1978; Meaburn & Walsh 1985).

Mz 3 is often compared with the young planetary nebula M 2-9, which also has a bright nucleus and bipolar structure, but has been observed in greater detail in the optical and IR (Minkowski 1947; Allen & Swings 1972; Swings & Andrillat 1979; Balick 1989; Hora

★E-mail: nathans@casa.colorado.edu

†Visiting Astronomer at Cerro Tololo Inter-American Observatory, National Optical Astronomy Observatories, operated by the Association of Universities for Research in Astronomy, Inc., under cooperative agreement with the National Science Foundation.

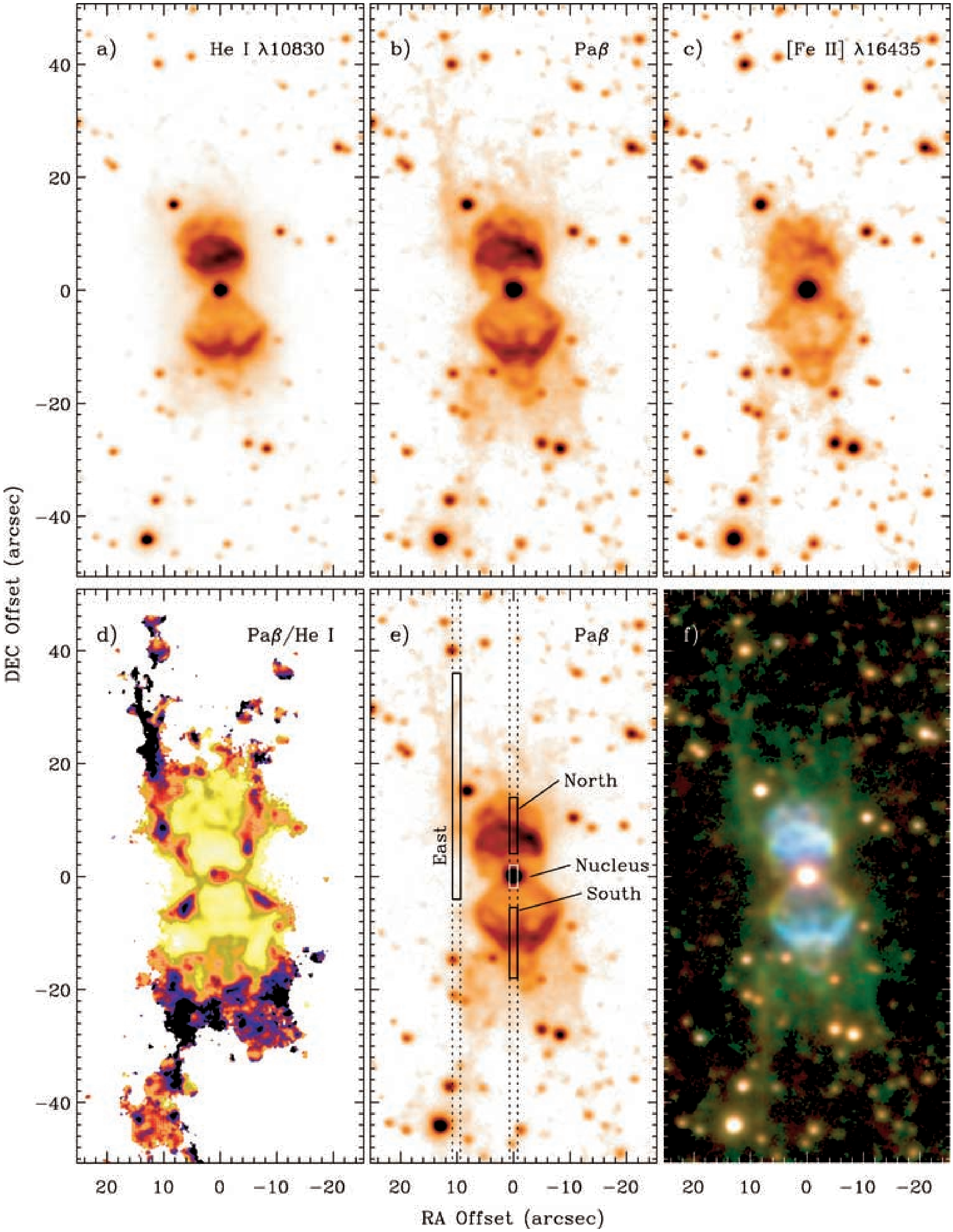

Figure 1. Near-IR imaging of Mz 3: (a) He I λ10 830, (b) hydrogen Paβ and (c) [Fe II] λ16 435. (d) The Paβ/He I λ10 830 flux ratio; blue and red areas have stronger Paβ and lower excitation, yellow areas have stronger He I and relatively high excitation. (e) Paβ image with slit positions superposed. (f) Composite three-colour image with He I λ10 830 in blue, Paβ in green and [Fe II] λ16 435 in red. Note, however, that Br12 contaminates the [Fe II] filter.

& Latter 1994; Doyle et al. 2000). Some authors have suggested that M 2-9, Mz 3 and similar objects such as He 2-104 might not be genuine planetary nebulae, and may instead be symbiotic binaries that had suffered recent mass ejections (Balick 1989; Corradi & Schwarz 1993; Corradi et al. 2000; Schmeja & Mineswenger 2001). Their progenitor stars may have had relatively high masses as well (Calvet & Peimbert 1983; Corradi 2000).

Limited portions of the optical spectrum of the polar lobes and nucleus of Mz 3 have been presented (Evans 1959; Cohen et al. 1978), but the near-IR spectrum has never been published. The purpose here is to provide optical spectra with better wavelength coverage and sensitivity than previous investigations, and to present the first near-IR images and spectra of Mz 3. Observations are presented in Section 2 and spectra of various positions are analysed in Sections 3–6. General conclusions are discussed in Section 7.

2 OBSERVATIONS

2.1 Imaging

Near-IR images of Mz 3 were obtained on 2001 March 8 using the Ohio State IR Imaging Spectrometer (OSIRIS) mounted on the CTIO 1.5-m telescope. OSIRIS has a 1024 × 1024 NICMOS3 array, with a pixel scale of 0.461 arcsec using the $f/7$ camera. Only a portion of the array is illuminated in this configuration, yielding a field of view of ∼5 arcmin. Narrow-band filters were used to image

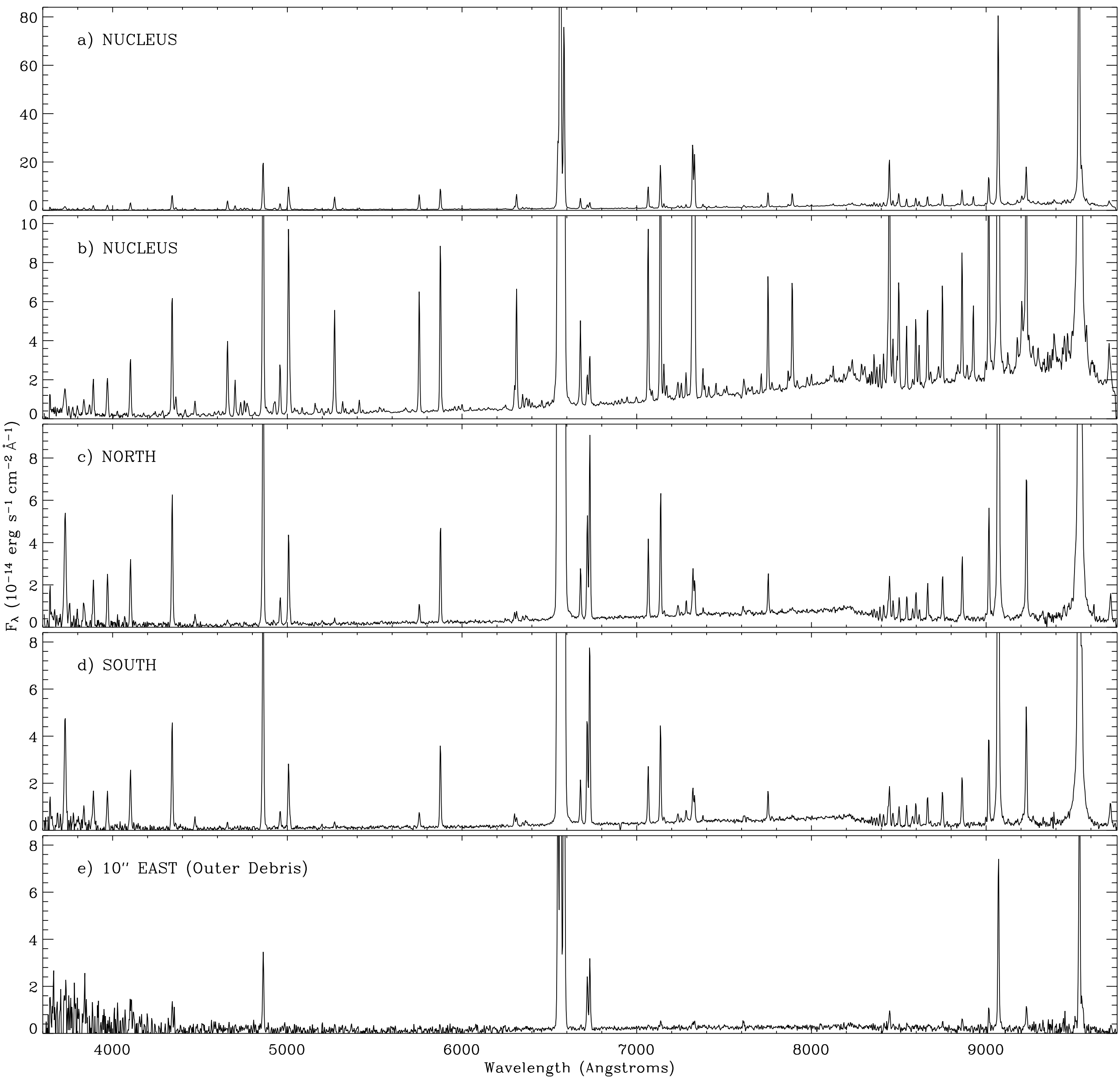

Figure 2. Optical spectra of Mz 3. (a) Spectrum of the bright nucleus region. (b) same as (a) at a different intensity scale. (c) The average northern polar lobe spectrum. (d) The average southern polar lobe spectrum. (e) The spectrum observed 10-arcsec east of the bright nucleus in the 'outer debris'. See Fig. 1(e) for slit positions.

Table 1. Summary of observations.

Date	Instrument	λ (Å)	Exp. time (s)	Comment
2001 Mar 8	OSIRIS	10 830	960	Image He I
2001 Mar 8	OSIRIS	12 819	960	Image Paβ
2001 Mar 8	OSIRIS	16 435	540	Image [Fe II]
2001 Mar 8	OSIRIS	21 220	480	Image H_2
2001 Mar 14	OSIRIS	10 000–11 600	480	*I*
2001 Mar 14	OSIRIS	11 800–13 900	1200	*J*
2001 Mar 14	OSIRIS	14 900–17 600	1200	*H*
2001 Mar 14	OSIRIS	19 600–23 200	1200	*K*
2002 Mar 1	RC Spec	6250–9700	1200	Star
2002 Mar 1	RC Spec	6250–9700	1200	10-arcsec E
2002 Mar 2	RC Spec	3600–7100	1200	Star
2002 Mar 2	RC Spec	3600–7100	1200	10-arcsec E

extended line emission from Mz 3 at He I λ10 830, Paβ, [Fe II] λ16 435 and H_2 2.122 μm, and each filter had a bandwidth of roughly 1 per cent of the wavelength. The images were obtained before morning twilight during semiphotometric conditions, so the absolute calibration was unreliable. Background sky emission was subtracted by chopping roughly 90 arcsec in a nearly east–west direction, keeping the object on the array. The actual chopping amplitude and direction were varied slightly with each exposure to correct for field stars included in the reference sky images. Individual exposure times were 120 s for each exposure in the He I and Paβ filters, and 60 s for each in the [Fe II] and H_2 filters. Several frames with slight positional offsets were obtained and then co-added for each filter, and the total integration times are given in Table 1.

No extended structure was detected in the H_2 filter, but Figs 1(a)–(c) show images obtained in the He I, Paβ and [Fe II] filters, respectively, where extended emission is striking. Fig. 1(d) is a false-colour image showing the ratio of Paβ to He I; red and blue areas denote relatively strong Paβ emission and yellow indicates stronger He I. Fig. 1(e) shows the Paβ image with spectroscopic apertures superposed (see below) and Fig. 1(f) shows a composite three-colour image with He I λ10 830 in blue, Paβ in green and [Fe II] λ16 435 in red. However, the reader should note that hydrogen Br12 contributes ~25 per cent of the emission in the [Fe II] filter.

2.2 Spectroscopy

2.2.1 *Optical spectroscopy*

Low-resolution ($R \sim$ 700–1600; 2-pixel) spectra from 3600 to 9700 Å were obtained on 2002 March 1 and 2 using the RC Spectrograph on the CTIO 1.5-m telescope. Long-slit spectra of Mz 3 were obtained with the 1.5-arcsec wide slit aperture oriented in the north–south direction (oriented close to the polar axis of Mz 3), centred on the bright central star and also at one position 10-arcsec east, as shown in Fig. 1(e). (A similar position 10-arcsec west was also observed, but the spectrum was not significantly different.) The pixel scale in the spatial direction was 1.3 arcsec. Spectra at each pointing were obtained on two separate nights in two different wavelength

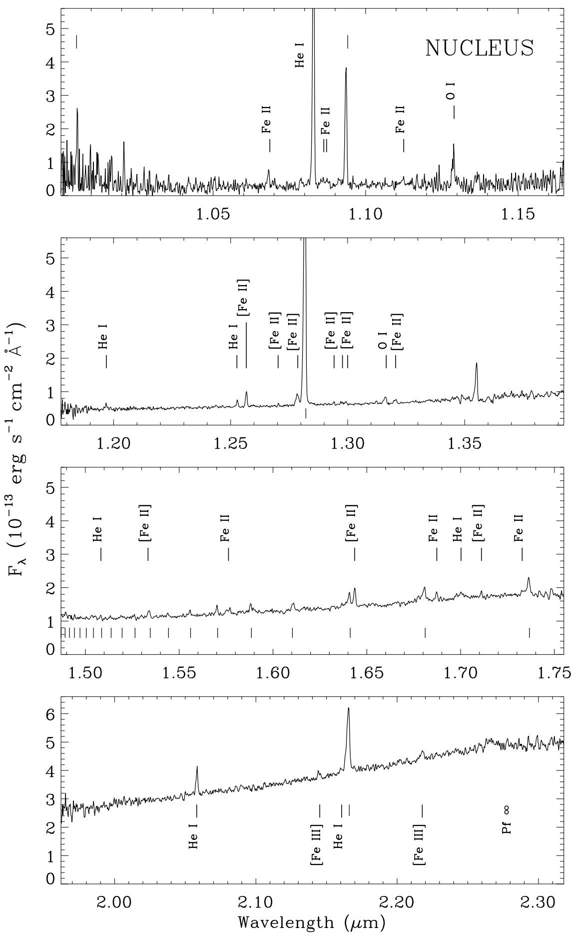

Figure 3. Infrared spectrum of the bright nucleus of Mz 3.

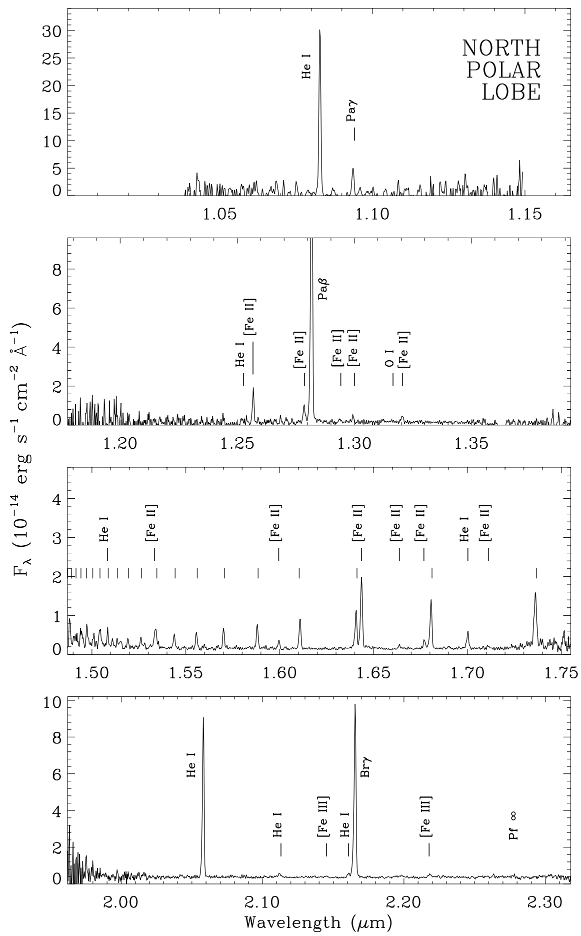

Figure 4. Infrared spectrum of the northern polar lobe.

ranges (blue, 3600–7100 Å and red, 6250–9700 Å), with total exposure times and other details listed in Table 1. Sky conditions were photometric; flux-calibration and telluric absorption correction (at red wavelengths) were accomplished using similar observations of the standard star LTT 3218.

In the resulting two-dimensional (2D) spectra, it was clear that the character of the spectrum changed as a function of position along the slit, with the bright nucleus showing many emission lines absent in either the northern or southern polar lobes. Spectra were extracted from a ∼4-arcsec segment of the slit centred on the nucleus, and larger segments of the slit in the northern and southern lobes and the east offset position, as shown in Fig. 1(e). The blue and red wavelength ranges of these extracted one-dimensional (1D) spectra were merged to form a single 3600–9700 Å spectrum with a common dispersion of 2.87 Å pixel^{-1} for each position; the average of the two was taken in the region around Hα where the blue and red spectra overlapped. The flux of the continuum from the central star in the separate blue and red spectra agreed to within the noise of the data in this overlapping region, indicating that the flux calibration and guiding were reliable. Fig. 2 shows the resulting spectra for the nucleus (2a and 2b, displayed at different intensity scales), the north (2c) and south (2d) polar lobes and the east offset position (2e).

2.2.2 Near-IR spectroscopy

Long-slit spectra of Mz 3 were obtained in the *I*, *J*, *H* and *K* infrared bands (1–2.3 μm) using OSIRIS mounted on the CTIO 4-m telescope on 2001 March 14. Spectra were obtained in high-resolution mode ($R \sim 3000$) with a 0.5-arcsec slit and a spatial pixel scale of 0.161 arcsec. The slit aperture was oriented in the north–south direction, but only at one pointing centred on the nucleus. Sky subtraction was accomplished by chopping 45 arcsec along the slit. Sky conditions were clear, and telluric correction and flux calibration were performed with reference to the bright star HR 3570. Other details are given in Table 1.

Along the slit passing through the nucleus, 1D spectra were extracted in the same spatial segments as for the optical spectra described above, as indicated in Fig. 1(e). Note, however, that the two slits had different widths, so a direct comparison of optical and IR fluxes for *extended* emission is compromised. Fig. 3 shows spectra in the *I*, *J*, *H* and *K* bandpasses for the nucleus, and Figs 4 and 5 show IR spectra for the northern and southern lobes. Spectra in the *I* band are of poor quality compared with other IR bandpasses because the *I*-band filter of OSIRIS has low efficiency, and because shorter total integrations were used as twilight approached, but these give information concerning the bright He I λ10 830 line.

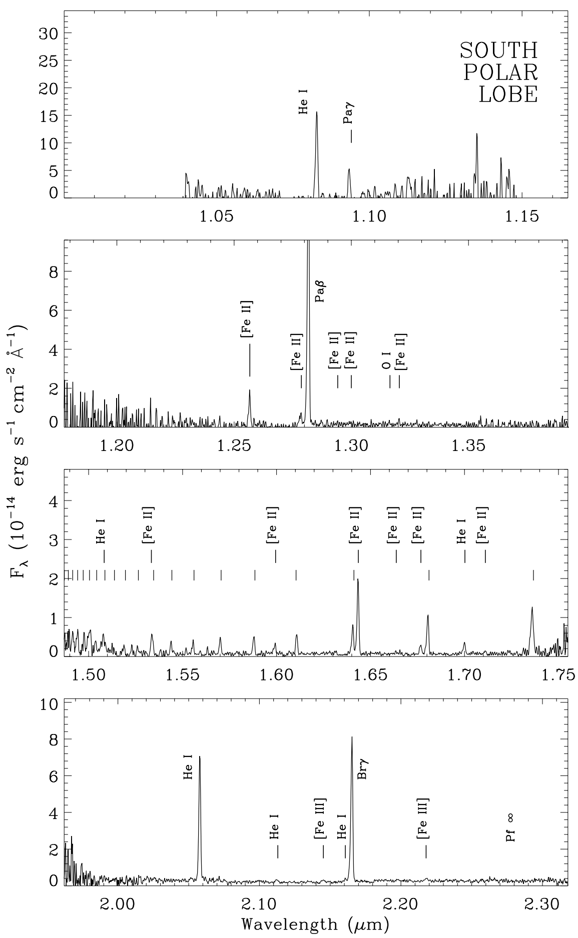

Figure 5. Infrared spectrum of the southern polar lobe.

3 SPATIAL DEPENDENCE OF EMISSION

IR images of Mz 3 in Fig. 1 show a striking morphology with apparently hollow, limb-brightened bipolar lobes. Recent *Hubble Space*

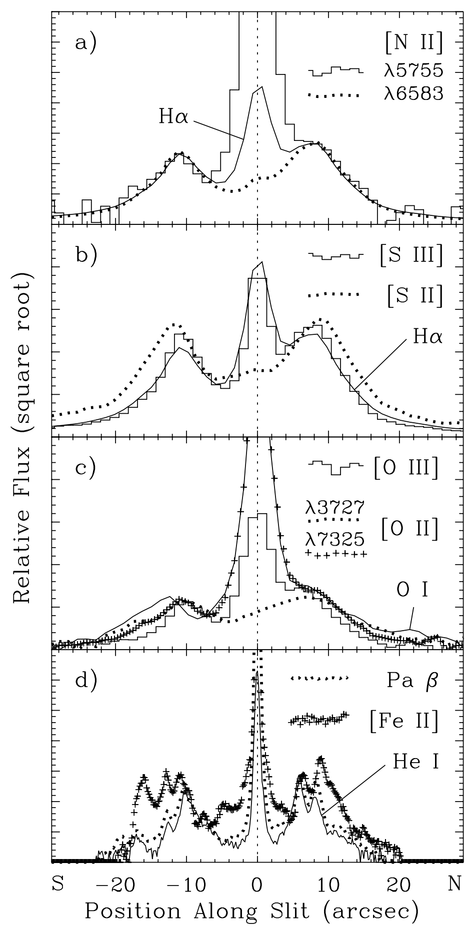

Figure 6. Distribution of emission along the slit passing through the nucleus. (a) [N II] λ5755, [N II] λ6583 and Hα. (b) [S III] λ9069, [S II] (λ 6717 + λ 6731) and Hα. (c) [O III] λ5007, [O II] λ3727, [O II] λ7325 and O I λ8446. (d) IR lines: Paβ, [Fe II] λ16 435 and He I λ20 581. Continuum emission was subtracted.

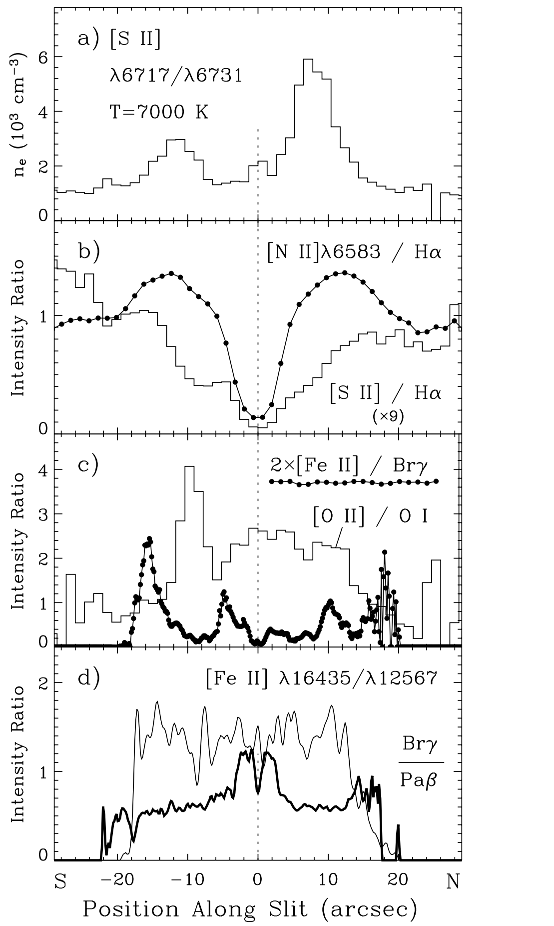

Figure 7. Line ratios as a function of position along the slit passing through the nucleus. (a) Electron density derived from the [S II] λ6717/λ6731 ratio on a linear scale. (b) [N II] λ6583/Hα ratio, and the [S II] (λ 6717 + λ 6731)/Hα ratio. (c) The [Fe II] λ16 435/Brγ flux ratio multiplied by a factor of 2 and the [O II] λ7325/O I λ8446 flux ratio. These ratios are sensitive to excitation. (d) Line ratios sensitive to reddening: [Fe II] λ16 435/λ12 567, and hydrogen Brγ/Paβ. All line ratios are displayed as observed, not corrected for reddening and the continuum was subtracted.

Telescope (*HST*) images provide better fuel for discussing morphology; compared with *HST* images (Balick 2000; Redman et al. 2000),[1] the Paβ image in Fig. 1(b) shows the same general structure in less detail, but the nucleus is relatively brighter at IR wavelengths. The present discussion will be limited to relative intensities of emission lines along the polar axis of the nebula, and clues to physical conditions derived from them. Figs 6 and 7 summarize the spatial distribution of some optical/IR line intensities and line ratios, respectively, along the polar axis of Mz 3; general characteristics are enumerated below. (Figs 6 and 7 also give important clues to the nature of the nucleus, but this discussion is postponed to Section 5.)

(i) *Intermediate ionization.* Most bright emission lines in the polar lobes of Mz 3, such as Hα, [N II], [S III], [O II], and others not shown in Fig. 6 (collisionally excited lines from ions between 13.6 and approximately 30 eV), have similar intensity distributions along the slit.

(ii) *High ionization.* A few emission lines such as [O III] and recombination lines of He I have a spatial distribution only slightly different from Hα in the polar lobes. They are somewhat weaker at larger distances from the star; this characteristic is seen best in the comparison of the near-IR lines He I λ20 581 and Paβ in Fig. 6(d) (the IR spectra have better spatial resolution than the optical data).

(iii) *Low ionization.* Some emission lines, such as O I, [S II] and [Fe II], are enhanced compared with hydrogen at larger distances from the nucleus. Again, this is most evident for IR lines in Fig. 6(d). These ions trace low-excitation regions where hydrogen has a larger neutral fraction, so it makes sense that they are enhanced further from the ionizing source. Low-excitation lines are most clearly enhanced just beyond the brightest part of the polar lobes, near the features that resemble 'blisters' protruding from the apex of each of the polar lobes (Fig. 1). These 'blisters' have a slightly red colour in Fig. 1(f), indicating relatively strong [Fe II] emission. The observed morphology begs the question of whether or not shocks may contribute to their excitation, in which case low-excitation emission would trace the dense cooling zone behind the shock.

Fig. 6(d) also shows enhanced [Fe II] emission compared with Paβ at distances relatively *close* to the central star, within ±6 arcsec. This does not fit the picture described immediately above, with low-excitation lines enhanced *further* from the nucleus. Since these enhanced [Fe II] regions near the star appear red in the colour image in Fig. 1(f), and since [Fe II] λ16 435 is at a longer-wavelength than Paβ and He I λ10 830, this is related to the broader question of whether the strong colour variations in Fig. 1(f) are due primarily to variations in extinction or excitation. Reddening-sensitive line ratios in Fig. 7(d) show no major variations in colour due to extinction across the polar lobes (at least not commensurate with the colour variations in Fig. 1f), suggesting that strong colour variations in Fig. 1(f) delineate regions of different excitation conditions instead.[2] The Paβ/He I ratio image in Fig. 1(d) supports this claim; regions that are coded as blue show relatively strong Paβ and presumably areas of lower excitation than areas coded yellow, where He I λ10 830 is strong. The low-excitation regions in Fig. 1(d) are found in the outer debris, the southern 'blister' at the apex of the southern polar lobe, and the limb-brightened side-walls of the polar lobes. Thus, the enhanced [Fe II] within 6 arcsec of the nucleus seen in the slit oriented along the polar axis may represent similar low-excitation material in near or far side-walls of the hollow polar lobes.

4 EMISSION FROM THE POLAR LOBES

Although variation in relative line intensities is seen along the slit aperture, Fig. 6 shows a minor positional dependence at the location of the brightest emission roughly 8-arcsec north of the nucleus. This is true for most emission lines, but Figs 6 and 7 indicate that caution is obviously needed at opposite extremes of excitation, such as [O III], He I, O I, [S II] and [Fe II]. With that in mind, it is worthwhile to consider average physical conditions derived from the integrated optical/IR spectrum of the northern lobe. Figs 1(c) and (d), and Figs 4 and 5 imply that spectra of the northern and southern lobes are virtually identical, so conclusions drawn from the analysis of the brighter northern lobe probably apply for both – especially the

[1] See also http://oposite.stsci.edu/pubinfo/pr/2001/05/

[2] However, the Brγ/Paβ ratio in Fig. 7(d) shows higher reddening within ±3 arcsec of the central star, which may suggest the presence of an obscuring disc or torus (see Section 7.2). The [Fe II] λ16 435/λ12 567 ratio is also sensitive to reddening; it is rather noisy, but it shows no drastic changes in reddening. The [Fe II] lines may be formed outside the dusty obscuring region (as noted above), and the hydrogen lines may be formed in the interior of the nebula.

Table 2. Northern lobe line intensities.

λ (Å)	ID	Observed	Dereddened
3726, 29	[O II]	43.16	72.74
3750	H12	5.771	9.672
3771	H11	2.831	4.720
3785	He I	0.942	1.565
3798	H10	1.947	3.224
3835	H9	4.847	7.950
3869	[Ne III]	1.137	1.847
3889	H8, He I	9.269	14.97
3970	Hϵ	11.33	17.84
4026	He I	1.479	2.283
4069, 76	[S II]	3.258	4.950
4102	Hδ	17.41	26.11
4340	Hγ	35.21	47.38
4363	[O III]	0.332	0.441
4387	He I	0.474	0.622
4471	He I	3.304	4.149
4658	[Fe III]	3.133	3.536
4702	[Fe III]	1.129	1.241
4755	[Fe III]	1.582	1.685
4814	[Fe III]	1.204	1.238
4861	Hβ	100.0	100.0
4889	[Fe II]	0.696	0.684
4906	[Fe II], [Fe IV]	0.489	0.475
4922	He I	1.213	1.169
4959	[O III]	7.249	6.834
5007	[O III]	25.46	23.32
5041	Si II	0.494	0.443
5056	Si II	0.457	0.406
5159	[Fe II]	0.640	0.536
5199	[N I]	1.425	1.166
5270	[Fe III]	1.641	1.290
5538	[Cl III]?	0.931	0.631
5661	[Fe II]	0.341	0.216
5676, 80	N II	0.548	0.345
5712	N II	0.314	0.194
5755	[N II]	5.150	3.122
5876	He I	23.43	13.35
5913	[Fe II]	0.614	0.343
5932, 40, 42	N II	0.685	0.379
6243	Fe II	0.620	0.293
6262	[Fe II]	0.535	0.251
6300	[O I]	1.972	0.907
6312	[S III]	2.159	0.987
6347	Si II	1.103	0.495
6364	[O I]	1.090	0.485
6371	Si II	0.874	0.387
6417	Fe II	0.332	0.143
6456	Fe II	0.236	0.100
6548	[N II]	485.6	195.9
6563	Hα	1157	463.1
6583	[N II]	1432	566.9
6678	He I	11.91	4.472
6717	[S II]	24.29	8.922
6731	[S II]	43.04	15.68
7065	He I	17.77	5.295
7136	[Ar III]	30.25	8.613
7155	[Fe II]	1.302	0.366
7172	[Fe II]	0.333	0.092
7237	C II	3.607	0.961
7256	[Ni II]	0.824	0.216
7281	He I	2.808	0.726
7319, 20	[O II]	10.07	2.539
7330, 31	[O II]	8.490	2.125
7379	[Ni II]	0.969	0.234
7389	[Fe II]	0.236	0.056
7412	[Ni II]	0.497	0.117
7612	[Ni II], [Fe II]	2.879	0.590
7642	?	2.331	0.468
7716	He I, [Cr II]	0.532	0.101
7751	[Ar III]	9.053	1.678
7774	O I	0.663	0.120
7826	He I, Fe II	1.057	0.185
7887	[N I], [Ni III]	3.162	0.529
8334	Pa24	0.612	0.073
8346	Pa23	0.983	0.116
8359	Pa22	1.802	0.211
8375	Pa21	1.453	0.168
8392	Pa20	2.269	0.260
8413	Pa19	3.726	0.421
8438	Pa18	1.211	0.134
8446	O I	12.26	1.353
8467	Pa17	4.177	0.454
8502	Pa16	5.511	0.584
8545	Pa15	5.333	0.548
8579	[Cl II], [V II]	2.710	0.272
8598	Pa14	6.734	0.667
8617	[Fe II]	2.370	0.231
8665	Pa13	7.651	0.724
8680, 3, 6	[N I]	3.295	0.308
8750	Pa12	10.58	0.947
8863	Pa11	16.98	1.415
9000	He I, [V II]	2.974	0.228
9015	Pa10	28.11	2.143
9069	[S III]	374.2	27.71
9229	Pa9	43.66	2.960
9268	[Fe II]	1.774	0.117
9445	[Fe III]	4.490	0.271
9532	[S III]	1263	73.15
9546	Pa8	16.19	0.929
9615	Fe II	2.974	0.164
9711	[Fe II]	9.808	0.517

Table 3. Northern lobe IR line intensities.

λ (Å)	ID	Observed	Dereddened
10 686	Fe II	13.78	30.65
10 751	?	11.79	25.48
10 830	He I	129.5	270.6
10 872	Fe II	6.652	13.65
10 938	H I Paγ	24.78	49.46
12 430	Fe I	1.702	1.934
12 528	He I	2.500	2.749
12 567	[Fe II]	9.919	10.76
12 788	[Fe II]	4.591	4.635
12 818	H I Paβ	100.0	100.0
12 943	[Fe II]	1.484	1.426
12 978	[Fe II], He I	1.920	1.825
13 206	[Fe II]	2.584	2.290
14 921	He I	1.300	0.726
14 938	H I Br26	1.592	0.885
14 967	H I Br25	1.444	0.797
15 001	H I Br24	1.534	0.841
15 039	H I Br23	2.270	1.233
15 083	He I, Br22	1.906	1.025
15 110	?	0.872	0.466
15 134	He I, Br21	1.696	0.901
15 192	H I Br20	1.162	0.609
15 260	H I Br19	2.421	1.249
15 335	[Fe II], Br18	5.643	2.862
15 439	H I Br17	2.219	1.099
15 556	H I Br16	2.617	1.264
15 700	H I Br15	3.155	1.476
15 849	Fe II	0.356	0.161
15 880	H I Br14	3.861	1.739
15 995	[Fe II]	1.466	0.644
16 109	H I Br13	4.917	2.112
16 407	H I Br12	7.000	2.832
16 435	[Fe II]	13.50	5.434
16 638	[Fe II]	0.834	0.322
16 769	[Fe II]	1.525	0.575
16 806	H I Br11	10.07	3.776
16 873	Fe II	0.435	0.161
17 002	He I	3.341	1.207
17 111	[Fe II]	0.718	0.254
17 362	H I Br10	17.32	5.871
17 449	[Fe II]	1.125	0.375
17 552	Fe II	3.339	1.095
20 581	He I	69.39	14.73
21 120	He I	3.468	0.691
21 366	?	0.686	0.133
21 451	[Fe III]	1.063	0.204
21 607	He I	1.711	0.323
21 655	H I Brγ	83.11	15.62
22 178	[Fe III]	2.530	0.450

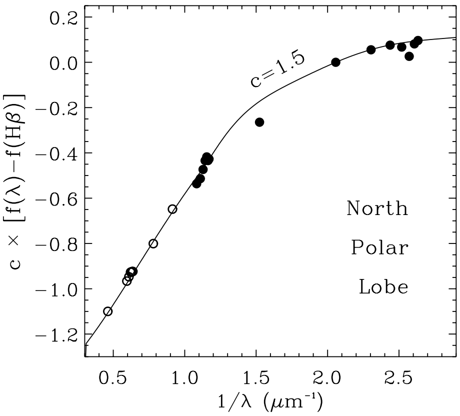

Figure 8. Reddening for the northern polar lobe. Solid dots show the reddening for optical hydrogen lines relative to Hβ and unfilled dots are for near-IR hydrogen lines. Reddening for IR lines was measured relative to Paβ and scaled, since the data were obtained with a different aperture size. The solid line shows the Galactic extinction law of Cardelli et al. (1989) for $c = 1.5$.

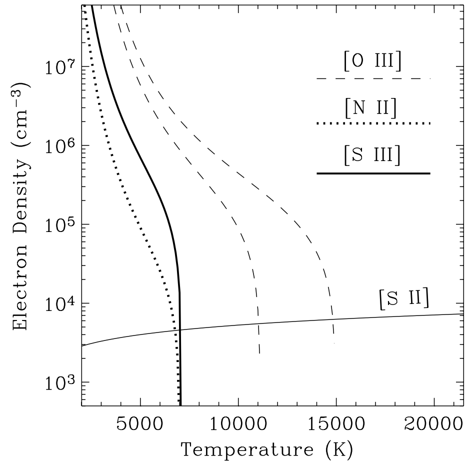

Figure 9. Curves for electron density as a function of temperature corresponding to the dereddened line ratios of [O III], [N II] and [S III]. The electron density derived from [S II] λ6717/λ6731 is also shown. The range of T_e for [O III] depends on how much [Fe II] λ4358 contaminates the [O III] λ4363 line (see the text).

regions that appear blue–green in Fig. 1(f). Relative intensities of optical lines in the northern polar lobe are listed in Table 2 and IR lines in Table 3.

4.1 Reddening

The observed spectrum of the northern lobe covers a wide wavelength range, and relative intensities of several hydrogen lines can be used to estimate extinction and reddening toward Mz 3. Assuming the intrinsic line intensities relative to Hβ denoted $I_0(\lambda)/I_0(\mathrm{H}\beta)$ are those for case B recombination with $n_e = 10^4$ cm^{-3} and $T_e = 10^4$ K computed by Hummer & Storey (1987), the observed value $I(\lambda)/I(\mathrm{H}\beta)$ can be used to estimate the logarithmic extinction c at $\lambda = 4861$ Å using the standard convention

$$c[f(\lambda) - f(\mathrm{H}\beta)] = \log_{10}\left[\frac{I(\lambda)/I(\mathrm{H}\beta)}{I_0(\lambda)/I_0(\mathrm{H}\beta)}\right], \quad (1)$$

where $f(\lambda)$ is the adopted reddening law. Fig. 8 shows observed hydrogen lines in the northern polar lobe. The solid line in Fig. 8 is the Galactic interstellar extinction law of Cardelli, Clayton & Mathis (1989) for a value of $c = 1.5$. This agrees well with the data, excluding Hα, which is usually stronger than case B values, and H8, which may be contaminated by He I λ3889. The logarithmic Hβ extinction of $c = 1.5$ is equivalent to $E(B - V) = 1.04$ and $A_V = 3.2$ mag, if $R = 3.1$. This extinction was used to calculate dereddened relative line intensities listed in Tables 2 and 3.

IR hydrogen lines are also plotted in Fig. 8, but the good agreement with $c = 1.5$ is somewhat fortuitous; the IR spectra were obtained with a narrower slit than the optical data, so line ratios relative to Paβ are scaled for comparison. Even so, the relative IR line ratios are consistent with the same reddening law. However, a discrepancy arises in the [Fe II] λ12 567/λ16 435 ratio, which depends only on atomic physics and acts as an independent reddening diagnostic. The intrinsic λ12 567/λ16 435 ratio is expected to be ∼1.36 (Nussbaumer & Storey 1988), and the reddening-corrected value in Table 3 is 1.98, which might suggest that $c \approx 1.5$ is an overestimate. One possible solution to this inconsistency is that the [Fe II] emission is formed outside the primary hydrogen emission region, perhaps in the 'blisters' at the extremes of the lobes as implied by Fig. 6(d), and that this outer [Fe II] zone suffers less extinction. The observed λ12 567/λ16 435 ratio is consistent with $c \approx 1.2$ or $A_V \approx 2.6$. This suggests that at least a third of the logarithmic extinction is local to Mz 3, rather than interstellar.

4.2 Electron density and temperature

Dereddened relative line intensities in Tables 2 and 3 can be used to estimate values for the average electron density n_e and the temperature T_e in the northern polar lobe. Fig. 7(a) shows the variation in n_e along the slit, derived from the observed [S II] λ6717/λ6731 intensity ratio. This is calculated assuming $T_e = 7000$ K (see below), although this assumption is not critical because the density calculated from [S II] lines is nearly independent of T_e. These results for n_e are similar in character but differ somewhat in detail compared with Lopez & Meaburn (1983). Fig. 9 shows the average n_e in the northern polar lobe for the observed value of [S II] λ6717/λ 6731 = 0.57. Figs 7(a) and 9 indicate that n_e in the northern lobe is roughly 4000–5000 cm^{-3}. This is probably a fair estimate since it is below the regime $n_e > 10^4$ cm^{-3} where the [S II] ratio becomes degenerate. Also, if the [S II] lines were not representative of the dominant electron density because of ionization or collisional de-excitation, one would not expect the regions of highest n_e in Fig. 7(a) to coincide with the brightest nebular emission in other species.

Temperature-sensitive line ratios of p^2 ions [O III] (λ4959 + λ5007)/λ4363, [N II] (λ6548 + λ6583)/λ5755 and [S III] (λ9069 + λ9532)/λ6312 have dereddened values of roughly 69, 244, and 160, respectively, in the northern lobe (these ratios are accurate to within approximately 5 per cent, except for [O III], see below). Values of n_e and T_e consistent with these ratios are plotted in Fig. 9 (using relations given by Smith et al. 2002, derived from information in Osterbrock 1989), along with the density derived from [S II] lines. Most emission from the northern lobe is consistent with $n_e = 4500 \pm 500$ cm^{-3} and $T_e = 7000 \pm 200$ K. This agrees with Fig. 6, which shows that Hα, [N II] and other prominent lines have similar distributions. (Important exceptions are low ionization potentials, as noted in Section 3.)

However, Fig. 9 indicates that [O III] emission traces somewhat hotter gas around 10 000–15 000 K. The higher [O III] temperature is uncertain, however, because it depends on how much the unresolved

[Fe II] λ4358 line may contribute to the measured [O III] λ4363 intensity; the two T_e curves for [O III] in Fig. 9 are drawn assuming that [Fe II] contributes either half or none of the λ4363 emission. [O III] emission in Mz 3 is unusual in that diffuse [O III] is not limited to the nucleus, but has a distribution only marginally resolved from other emission lines such as hydrogen in Fig. 6. Although it may reside closer to the star, [O III] emission still clearly comes from gas in the bright regions of the polar lobes. One might expect the [O III] distribution to resemble that of He I emission, shown in blue in Fig. 1(f), which seems concentrated toward high latitudes in the bipolar nebula. Thus, [O III] and He I probably trace a higher ionization skin on the inner surfaces of hollow bipolar lobes with a relatively unobstructed view of the central engine. Based on Fig. 1(f), this zone appears to be concentrated toward latitudes more than $\sim 45^\circ$ from the equator.

Some IR lines present a different picture of the physical conditions in the polar lobes. Specifically, [Fe II] line ratios λ15 335/λ16 435, λ15 995/λ16 435 and λ16 638/λ16 435 correspond to transitions from a ^{4}D levels closely spaced in energy and are good density indicators (Nussbaumer & Storey 1988). Observed ratios for these lines in Table 3 indicate electron densities of roughly 10 000–15 000 cm^{-3} (note that λ15 335 needs to be corrected for Br 18 emission). This is twice the highest density in the polar lobes traced by [S II]. The strongest [Fe II] λ16 435 emission comes from material outside the brightest optical emission, and may best trace the 'blisters' at the ends of the lobes. Higher densities and lower excitation there may suggest compression and heating by shocks due to fast material at the polar axes impacting the lobes. In fact, this is the same position where Redman et al. (2000) observed high-velocity Doppler-shifted features. The [Fe II] λ16 435/Brγ ratio is strongly enhanced at these same positions (Fig. 7c), with reddening-corrected values reaching ~ 3. H II regions typically have ratios of less than 1, whereas shock sources such as supernova remnants have λ16 435/Br$\gamma \gtrsim 30$ (Graham, Wright & Longmore 1987). Thus, emission from the polar blisters of Mz 3 may represent a mix of shocks and radiative excitation.

4.3 Excitation and chemical abundances

Since the polar lobes of Mz 3 show stratified ionization and physical conditions, analytical estimates of the chemical abundances are not straightforward. The comprehensive spectral synthesis code CLOUDY (Ferland 1996) was used to simulate the dereddened spectrum of the lobes with assumptions concerning the geometry and density gleaned from the analysis above. The geometry was approximated as the polar part of a thick spherical shell with $R = 1.8 \times 10^{17}$ (D^2_{kpc}) cm, thickness $\Delta R = 5 \times 10^{16}$ (D^2_{kpc}) cm, average electron density $n_e = 5000\ \mathrm{cm}^{-3}$ and density fluctuations of a factor of 2 (the inhomogeneous density structure is apparent in images).

To reproduce the dereddened observed spectrum of the northern polar lobe, an ionization source (presumed to be a blackbody) with $T = 36\,000$ K and $L = 10\,000\ \mathrm{L}_\odot$ yielded the best results. This temperature is hotter than the 32 000-K source derived by Cohen et al. (1978), but was needed to account for the observed strength of He I lines in the optical and IR. Models that varied by more than ±2000 K or ±500 $\mathrm{L}_\odot$ gave obviously discrepant relative line intensities. For example, for higher temperatures the [O III] lines were a factor of 2 too strong, and for lower temperatures He I lines were far too weak, even with extremely high He abundances. The model yielded a volume-averaged electron temperature of ~ 6900 K, consistent with the analytical estimate in Fig. 9. The simulated spectrum reproduced line intensities in Tables 2 and 3 remarkably well – intensities of all bright lines in the optical/IR spectrum were matched to within 5 per cent, with a few caveats. Intensities of the following lines were underestimated with the percentage of the observed flux indicated in parentheses: [O II] λλ3726, 3729 (60 per cent; even though [O II] λλ7320, 7330 was reproduced accurately), [N I] λ5200 (60 per cent), [O I] λλ6300, 6363 (85 per cent), [S II] λλ6717, 6731 (65 per cent), and [Fe II] λ12 567 and λ16 435 (30 per cent). However, these few discrepancies with the model are not a cause for grave concern, since all of these lines are typically enhanced in shocks, and all are seen to be stronger beyond the bright polar lobes in the 'blisters' (included in the aperture).

Dereddened line strengths could not be reproduced in the model without modifying default 'H II region' abundances of CLOUDY, which include grain depletion (see Ferland 1996). The chemical abundances constrained by the present set of observations, on a log scale with H = 12, are: He = 11.3, N = 8.67, O = 8.64, Ne = 7.78, Si = 6.6, S = 7.08, Ar = 6.68 and Fe = 7.1 (the carbon abundance is not constrained by this calculation or the present observations – UV spectra are needed). These are total gas-phase abundances, including all ionization stages calculated self-consistently, with no uncertain ionization correction factors. Both He and N needed to be increased significantly from the default values; He by a factor of ~ 2 (helium was 80 per cent neutral and hydrogen was 60 per cent neutral, adding uncertainty), and N by a factor of 6.6. Iron is also enhanced, presumably due to Fe being liberated by grain destruction into the gas phase. The strong enhancements of N and moderate He enrichment qualitatively agree with some earlier studies (Cohen et al. 1978; Calvet & Peimbert 1983; Liu et al. 2001), but not with Zhang & Liu (2002), who find no evidence for He enrichment.[3] The He and N enrichment in Mz 3 is high but consistent with models of thermal-pulsing asymptotic giant branch (AGB) stars with intermediate main-sequence masses between approximately 3 and 8 $\mathrm{M}_\odot$ (Henry, Kwitter & Buell 1998; Kwitter & Henry 2000). Thus, bipolar nebulae such as Mz 3 and similar objects may have evolved from symbiotic binaries with progenitors somewhat more massive than the Sun (Calvet & Peimbert 1983; Corradi 2000). S/O and Ar/O are both enhanced by roughly a factor of ~ 2 compared with a sample of planetaries (Kwitter, Henry & Milingo 2003).

Shock excitation? The simulated spectrum above is based on the assumption that radiative excitation dominates the energy balance, but several clues suggest that shock heating also plays a role in some parts of the nebula. A relevant quantity is the ratio of radiative to kinetic luminosity ξ given crudely by

$$\xi \equiv \frac{2L}{\dot{M} v^2} = \frac{L}{2\pi R^2 m_{\mathrm{H}} n_e v^3}, \tag{2}$$

where L is the UV luminosity of the exciting source, m_{H} is the proton mass, $n_e \approx 5000\ \mathrm{cm}^{-3}$ is the electron density in the lobes, $R \approx 1.8 \times 10^{17}$ cm is the radius of the lobes, and v is the relative shock velocity. If the expanding lobes are the source of mechanical energy and we assume a characteristic shock velocity[4] of $\sim 90\ \mathrm{km\ s^{-1}}$ (Meaburn & Walsh 1985), we find that $\xi > 10$. If, on the other hand, we adopt the more likely scenario that shocks would be caused by a fast stellar wind (with $v_\infty = 500\ \mathrm{km\ s^{-1}}$ and $\dot{M} = 10^{-5}\ \mathrm{M}_\odot\ \mathrm{yr}^{-1}$, for example) catching up with the insides of the polar lobes, then we still have

[3] However, their assumed He ionization correction factor was scaled from S^+ and S^{++}, even though their S^{++} value came from the faint [S III] λ6312 line instead of [S III] λλ9069, 9532.

[4] Note that v is the *relative* shock velocity, i.e. the difference between the lobes themselves and slower material they ram into.

Table 4. 10-arcsec east line intensities.

λ (Å)	ID	Observed	Dereddened
4340	Hγ	38.40	49.07
4861	Hβ	100.0	100.0
4889	[Fe II]	8.853	8.733
6548	[N II]	360.2	170.2
6563	Hα	1038	487.3
6583	[N II]	1193	555.3
6678	He I	6.166	2.744
6717	[S II]	62.85	27.49
6731	[S II]	91.20	39.62
7065	He I	4.884	1.795
7136	[Ar III]	11.60	4.113
7325	[O II]	15.21	4.857
7612	[Ni II]	11.61	3.142
8446	O I	23.27	3.769
8750	Pa12	6.741	0.918
8863	Pa11	10.88	1.398
9015	Pa10	20.27	2.419
9069	[S III]	230.2	26.81
9229	Pa9	28.47	3.081
9532	[S III]	485.1	45.99

$\xi > 10$. Thus, for most of the polar lobe emission, radiative excitation probably dominates the energy balance. However, if dense high-velocity gas (a jet?) interacts with the lobes at certain positions, such as the 'blisters' near the polar axis, one might expect that shocks could be important. The blister atop the northern polar lobe contributes some emission to the spectrum in Figs 2(c) and 4, so further work at high spatial resolution is needed.

5 OUTER DEBRIS

Images in Fig. 1 show faint emission from debris outside the well-defined polar lobes, extending to almost 40-arcsec north and south of the nucleus. These outer debris also appear somewhat limb-brightened, and the straight edges give the impression of walls of a large cylinder. Fig. 2(e) shows the optical spectrum of these outer debris obtained with the slit positioned 10-arcsec east of the central star as shown in Fig. 1(e). Observed line strengths are listed in Table 4.

Again, relative intensities of hydrogen lines can be used to estimate the reddening toward this material using the same method described earlier for the polar lobes. Hydrogen line intensities for the outer debris 10-arcsec east of the star are shown in Fig. 10, and are fitted with the reddening law of Cardelli et al. (1989) for a value of $c = 1.23$. The corresponding values of $E(B - V) = 0.85$ and $A_V = 2.65$ are lower than toward the brightest emission from the polar lobes, supporting the conjecture above that much of that reddening is local to Mz 3, rather than interstellar.

Lines from [O III] are not detected in the outer debris, and [N II] λ5755 and [S III] λ6312 are also too weak to be detected, so estimating the electron temperature from p^2 ions is difficult. Upper limits to [N II] λ5755 and [S III] λ6312 suggest electron temperatures below approximately 10 000 K. The electron density indicated by the [S II] λ6717/λ6731 ratio of 0.69 is between 2000 and 2300 cm^{-3}. This is not much higher than the values measured at large distances from the star in Fig. 7(a) for the slit passing through the nucleus.

Although the spectrum of the outer debris in Fig. 2(e) has a lower signal-to-noise ratio than spectra of the polar lobes, clear differences can be seen. For instance, relatively high excitation lines such as [O III] λ5007, He I λ5876 and [Ar III] λ7136 are nearly as bright as [S II] λ6717 in the polar lobes, but are clearly much weaker in the outer debris.

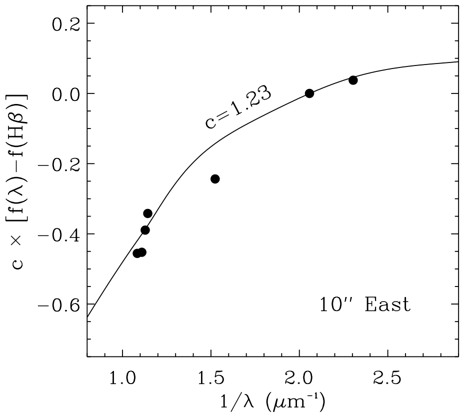

Figure 10. Same as in Fig. 8, but reddening for the hydrogen lines in outer debris sampled with the slit placed 10-arcsec east of the nucleus. Hydrogen lines from near-IR spectra are not included because IR spectra were not obtained at this offset position.

6 THE BRIGHT NUCLEUS

The spectrum of the bright nucleus of Mz 3 shows a dense forest of emission lines uncharacteristic of traditional planetary nebulae. Even at low dispersion, over 300 lines between 3600 and 23 000 Å are identified in Tables 5 and 6. Many of these come in close pairs or groups, so multiple Gaussian fits were applied to estimate the line intensities in certain cases. These nuclear emission lines indicate a wide range of ionization from O I and [Fe II] up to [O III] and He I. Aside from hydrogen, the spectrum is dominated by [S III], [N II], [Ar III], [O III], [O II], O I and He I, but perhaps the most defining characteristic of the nucleus is the strength of numerous [Fe III] lines seen throughout the spectrum. In this respect, the nuclear spectrum of Mz 3 resembles the nebular spectrum of RY Scuti (Smith et al. 2002), in which these lines were first identified (Merrill 1928). The nuclear spectrum of Mz 3 also shares some characteristics with symbiotic stars such as RR Tel, the nucleus of M 2-9, and even η Carinae.

6.1 Reddening

In the same way as described above for the northern polar lobe and outer debris, observed relative intensities of hydrogen lines in Tables 5 and 6 can be used to estimate extinction toward the bright nucleus of Mz 3. Fig. 11 shows the reddening toward the nucleus derived from hydrogen lines, plotted in the same way as in Figs 8 and 10 (except that case B values for $n_e = 10^6$ cm^{-3} from Hummer & Storey 1987 were used instead of $n_e = 10^4$; the difference is minor). The solid curve shows the Galactic reddening law of Cardelli et al. (1989) for a logarithmic Hβ extinction of $c = 2.16$, corresponding to $E(B - V) = 1.5$ and $A_V = 4.65$. Dereddened relative line intensities in the nucleus are also given in Tables 5 and 6.

Hα and H8 λ3889 deviate from the standard reddening law, as expected for the reasons mentioned earlier. As in Fig. 8, near-IR line intensities were first measured relative to Paβ, and then scaled to fit on the same curve for comparison with optical lines because different aperture widths were used in the two wavelength regimes. Considered independently, the near-IR hydrogen line intensities are

Table 5. Nucleus line intensities.

λ (Å)	ID	Observed	Dereddened
3704	H16	0.677	1.414
3712	H15	1.301	2.710
3726, 29	[O II]	9.623	19.95
3750	H12	1.663	3.422
3771	H11	2.003	4.092
3798	H10	2.560	5.181
3835	H9	4.098	8.182
3869	[Ne III]	2.534	4.993
3889	H8, He I	8.744	17.09
3970	Hϵ	10.07	18.99
3995	N II	0.522	0.972
4026	He I	1.033	1.895
4061	?	0.335	0.603
4069	[S II]	0.674	1.209
4076	[S II]	0.496	0.886
4102	Hδ	14.41	25.39
4121	He I	0.616	1.074
4144	He I, [Fe II]	0.468	0.805
4161	Fe II	0.143	0.243
4177	[Fe II]	0.864	1.457
4201	[Ni II]	0.610	1.013
4227	Ca I	0.917	1.499
4233	Fe II	0.732	1.192
4244	[Fe II]	1.212	1.959
4249	[Ni II]	0.354	0.570
4266	[Fe II], C II	1.229	1.958
4287	[Fe II]	2.345	3.684
4340	Hγ	30.49	46.18
4363	[O III]	3.331	4.963
4387	He I	0.981	1.436
4414	[Fe II]	1.960	2.813
4452	[Fe II]	0.693	0.966
4458	[Fe II]	0.696	0.966
4471	He I	3.666	5.040
4489	[Fe II]	0.679	0.920
4515, 20, 23	Fe II	1.397	1.856
4549	Fe II	0.357	0.461
4556	Fe II	0.329	0.423
4583, 4	Fe II	0.627	0.789
4607	[Fe III]	1.034	1.276
4629	Fe II	0.680	0.824
4640	[Fe II]	0.373	0.448
4658	[Fe III]	20.35	24.10
4702	[Fe III]	7.870	8.989
4713	He I	1.070	1.211
4734	[Fe III]	3.437	3.822
4755	[Fe III]	3.646	3.984
4769	[Fe III]	3.679	3.974
4778	[Fe III]	0.861	0.923
4814	[Fe III]	1.054	1.096
4861	Hβ	100.0	100.0
4881	[Fe III]	1.075	1.057
4889	[Fe III]	0.554	0.541
4906	[Fe II], [Fe IV]	0.420	0.404
4922	He I, Fe II	1.643	1.560
4931	[Fe III]	3.004	2.832
4959	[O III]	11.89	10.95
5007	[O III]	50.81	44.96
5029	[Fe III]	0.542	0.470
5041	Si II	1.568	1.348
5056	Si II	1.283	1.090
5085	[Fe III]	1.300	1.078
5112	[Fe II]	0.725	0.588
5159	[Fe II]	2.021	1.578
5169	Fe II	1.045	0.809
5200	[N I]	1.816	1.373
5220	[Fe II]	0.917	0.681

Table 5 – *continued*

λ (Å)	ID	Observed	Dereddened
5235	Fe II	1.596	1.172
5270	[Fe III]	27.17	19.41
5297	[Fe II]	0.129	0.090
5317	Fe II	2.939	2.023
5334	[Fe II]	1.049	0.712
5347	[Fe II]	0.176	0.118
5363	Fe II	0.901	0.598
5377	[Fe II]	1.109	0.728
5412	[Fe III]	2.922	1.869
5433	[Fe II]	0.886	0.557
5455	[Cr III], N II	0.121	0.074
5472	[Cr III], [Co III]	0.253	0.154
5477	[Fe II]	0.518	0.315
5496	[Fe II], N II	0.519	0.311
5507	[Cr III], Fe II	0.743	0.442
5528	[Fe II]	1.459	0.855
5535	Fe II	0.529	0.308
5552	[Cr III], [Fe II]	1.286	0.740
5568, 9	[V II], [Cr II]	0.479	0.272
5582	[Fe II]	0.531	0.299
5615	[V II]	0.194	0.106
5631	[Fe III]	0.131	0.070
5651	[Fe II]	0.528	0.282
5667	N II	0.273	0.144
5676, 80	N II	2.299	1.209
5696	Fe II, Si III	0.044	0.022
5718	[Fe II]	0.926	0.472
5726	[Fe II]	0.179	0.090
5755	[N II]	28.24	14.03
5799	[Fe II]	0.411	0.197
5823	[Cr III]	0.239	0.113
5835	[Fe II]	0.437	0.205
5876	He I	38.81	17.70
5905	[Ni IV]	0.521	0.232
5929, 32	N II	0.342	0.150
5940, 42	N II	0.205	0.089
5947	[Cr III]?	0.533	0.231
5958	Si II	0.983	0.423
5979	Si II	1.972	0.836
6000	[Ni III]	1.399	0.584
6045	[Fe II]	0.721	0.292
6067	[V II]?	0.116	0.046
6083	[Fe III]	0.116	0.045
6096	[Fe III]	0.486	0.189
6125	[Ni IV]	0.527	0.201
6140	[Fe III]	0.217	0.082
6148, 49	Fe II	0.743	0.279
6158	Fe II	0.236	0.088
6189	[Fe II]	0.363	0.132
6238	Fe II	1.247	0.440
6248	Fe II	1.519	0.532
6262	[Fe II]	0.408	0.141
6300	[O I]	7.469	2.524
6312	[S III]	25.42	8.517
6347	Si II	2.938	0.959
6364	[O I]	1.350	0.435
6371	Si II	3.210	1.030
6384, 5	Fe II	1.676	0.532
6401	[Ni III]	1.585	0.497
6417	Fe II	0.626	0.194
6433	Fe II	0.660	0.202
6441	[Ni II]	0.664	0.202
6456	Fe II	2.365	0.713
6485	[Fe II]	0.965	0.284
6491	Fe II	0.724	0.212
6506	Fe II	0.254	0.073
6516	Fe II	0.468	0.134

Table 5 – *continued*

λ (Å)	ID	Observed	Dereddened
6548	[N II]	119.5	33.62
6563	Hα	1833.	509.8
6583	[N II]	317.3	86.92
6612	[Fe IV]	0.235	0.062
6641	[Cr IV]	0.445	0.116
6667	[Ni II]	0.504	0.129
6678	He I	20.20	5.139
6717	[S II]	7.708	1.901
6731	[S II]	12.38	3.020
6747	[Fe II]	0.320	0.077
6793	[Fe IV]	0.877	0.203
6809	[Fe II]	0.532	0.121
6822	[V III]	0.223	0.050
6829	[Fe II]	0.300	0.067
6843	[Fe III]	0.141	0.031
6856	He I	0.104	0.022
6876, 7	[Co II], [V III]	0.840	0.182
6896	[Fe II]	0.613	0.130
6915	[Cr IV]	1.126	0.236
6943	Fe II	1.620	0.331
6997	[Fe IV]	1.625	0.317
7032, 4	[V II], [Ti III]	0.411	0.077
7065	He I	38.90	7.163
7078	[Ni II]	2.253	0.410
7088	[Fe III]	1.823	0.328
7111, 2	[Fe IV]	0.254	0.044
7136	[Ar III]	75.35	13.02
7155	[Fe II]	7.215	1.225
7172	[Fe II]	4.029	0.673
7184	[Fe IV]	0.853	0.141
7191, 3	[Fe IV]	1.260	0.207
7204	Fe II	0.313	0.050
7223,5	[Fe IV], Fe II	0.957	0.152
7237	[Ar IV]	4.487	0.706
7256	[Ni II]	3.331	0.515
7281	He I	4.455	0.673
7298	He I	0.461	0.068
7319, 20	[O II]	124.2	18.11
7330, 31	[O II]	80.18	11.57
7379	[Ni II]	7.134	0.982
7389	[Fe II]	1.710	0.233
7412	[Ni II]	2.677	0.357
7442	?	0.336	0.043
7453	[Fe II]	3.340	0.428
7468	[Fe IV]	0.560	0.070
7500	He I	1.991	0.243
7516	[Fe III]	2.385	0.287
7534	Fe II	0.177	0.020
7574	[Fe III]	0.659	0.074
7612	[Ni II], [Fe II]	4.868	0.532
7638	[Fe II]	2.502	0.266
7657	[Cr II]	2.319	0.242
7687	[Fe II]	0.899	0.091
7712	Fe II	3.649	0.360
7733	[Fe II]	0.381	0.036
7751	[Ar III]	24.76	2.349
7774	O I	1.824	0.169
7816	He I	0.844	0.074
7853	[Cr II]	0.185	0.015
7867	Fe II	4.566	0.384
7878	?	1.046	0.086
7890	[Ni III]	28.44	2.335
7918	Fe II	2.031	0.161
7976	Fe II	2.188	0.164
8000	[Cr II]	2.234	0.163
8023	[Fe II]	0.295	0.021
8031	Fe II	0.597	0.042
8060	[Ni III], [V II]	0.348	0.023
8084	Fe II	0.649	0.043
8091	Fe II	0.335	0.022
8107	Fe II, [Mn II]	3.596	0.234
8125	[Cr II]	3.975	0.254
8139	[Ti II]	0.331	0.020
8158	Fe II	0.678	0.041
8185, 8	N I	1.457	0.087
8214	[Fe III]	7.489	0.437
8233	[V II]?	8.750	0.500
8250	Fe II	1.104	0.062
8260	Fe II	0.454	0.025
8288	Fe II	5.254	0.284
8301	Pa28, [Ni II]	1.589	0.084
8306	Pa27, Fe II	2.017	0.107
8314	Pa26	0.862	0.045
8323	Pa25	0.612	0.031
8334	Pa24	1.548	0.079
8346	Pa23	2.105	0.107
8359	Pa22	6.565	0.329
8375	Pa21	3.640	0.179
8392	Pa20	4.261	0.206
8413	Pa19	11.28	0.536
8438	Pa18	19.77	0.916
8446	O I	79.16	3.640
8467	Pa17	13.44	0.605
8490	Fe II	10.22	0.449
8502	Pa16	25.44	1.105
8545	Pa15	11.95	0.497
8579	[Cl II], [V II]	1.691	0.068
8598	Pa14	16.29	0.644
8617	[Fe II]	9.324	0.362
8629	N I	0.799	0.030
8665	Pa13	18.80	0.697
8680, 3, 6	N I	3.008	0.110
8703	N I	0.428	0.015
8729	[Fe III]	6.742	0.235
8750	Pa12	20.75	0.711
8777	He I	0.876	0.029
8830	Cr II	0.746	0.023
8839	[Fe III]	5.797	0.183
8863	Pa11	32.00	0.993
8892	[Fe II]	4.195	0.127
8907	Cr II	0.626	0.018
8916	Cr II	1.011	0.030
8927	Fe II	17.79	0.523
8956	Fe II	1.152	0.033
8997	He I, [Fe IV]	2.212	0.061
9015	Pa10	62.39	1.710
9033	[Fe II]	0.567	0.015
9069	[S III]	393.3	10.35
9123	Fe II	6.529	0.164
9132	Fe II	3.265	0.081
9176, 8	Fe II	8.795	0.212
9203, 4	Fe II	38.52	0.913
9229	Pa9	87.55	2.036
9245	?	3.775	0.086
9268	[Fe II]	11.14	0.251
9298	Fe II	5.218	0.115
9386, 89, 93	Fe II, N I	9.110	0.188
9445	[Fe III]	4.977	0.098
9465	[Fe II]	5.594	0.109
9490,1	[Fe II], [Cr II]	2.668	0.051
9532	[S III]	1436	26.71
9546	Pa8	180.7	3.328
9573	Fe II	5.188	0.093
9609	[Fe III]	6.707	0.118
9702	[Fe III]	19.12	0.315

Table 6. Nucleus IR line intensities.

λ (Å)	ID	Observed	Dereddened
10 502	Fe II	1.717	5.876
10 608	[Fe III]	1.055	3.382
10 686	Fe II	4.051	12.37
10 700	?	1.859	5.630
10 788	?	2.777	7.975
10 830	He I	72.10	201.9
10 863	Fe II	6.354	17.44
10 913	He I	1.677	4.471
10 938	H I Paγ	27.42	72.03
11 126	Fe II	2.223	5.238
11 287	O I	10.17	21.87
11 969	He I	1.732	2.594
12 430	Fe I	0.810	0.968
12 438	N I?	0.807	0.961
12 528	He I	2.076	2.370
12 567	[Fe II]	3.970	4.451
12 703	[Fe II]	0.596	0.627
12 788	[Fe II]	3.946	3.999
12 818	H I Paβ	100.0	100.0
12 943	[Fe II]	0.689	0.652
12 978	[Fe II], He I	0.784	0.731
12 992	[Fe II]	0.867	0.803
13 123	?	0.662	0.579
13 165	O I	3.032	2.606
13 206	[Fe II]	1.904	1.608
13 550	?	11.81	8.656
15 001	H I Br24	0.484	0.209
15 039	H I Br23	1.341	0.571
15 083	He I, Br22	1.374	0.577
15 134	He I, Br21	1.235	0.510
15 192	H I Br20	1.920	0.778
15 260	H I Br19	1.501	0.595
15 335	[Fe II], Br18	3.673	1.422
15 439	H I Br17	1.705	0.639
15 556	H I Br16	2.736	0.989
15 700	H I Br15	2.977	1.030
15 758	Fe II	3.268	1.111
15 772	?	1.509	0.511
15 880	H I Br14	3.448	1.130
15 995	[Fe II]	1.354	0.429
16 109	H I Br13	4.398	1.349
16 407	H I Br12	9.793	2.765
16 435	[Fe II]	8.006	2.243
16 638	[Fe II]	1.637	0.434
16 769	[Fe II]	1.813	0.464
16 806	H I Br11	13.81	3.504
16 873	Fe II	3.721	0.927
17 002	He I	7.394	1.783
17 111	[Fe II]	1.646	0.386
17 338	Fe II	4.538	1.006
17 362	H I Br10	8.948	1.972
20 581	He I	16.05	1.841
20 888	Fe II	3.727	0.406
21 451	[Fe III]	6.237	0.622
21 607	He I	2.568	0.250
21 655	H I Brγ	90.84	8.787
22 178	[Fe III]	11.78	1.055

consistent with somewhat smaller reddening, with the caveat that the peak Brγ flux may be saturated for a few pixels.

In any case, the extinction of $A_V = 4.65$ measured separately for the nucleus of Mz 3 is critical, because it is much higher than the extinction toward other parts of the nebula. This result is qualitatively consistent with spatial variation in the Brγ/Paβ ratio across the major axis of the nebula (Fig. 7d), which indicates a marked increase

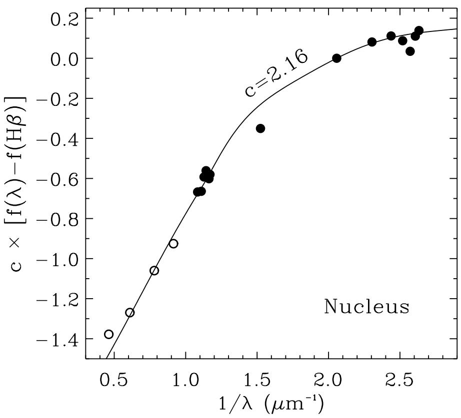

Figure 11. Same as in Fig. 8, but reddening for the bright nucleus of Mz 3. Again, near-IR lines are measured relative to Paβ and are scaled somewhat arbitrarily for comparison with extinction measured relative to Hβ.

in absorption within ±3 arcsec of the star. The most obvious interpretation of this larger extinction is that a dusty equatorial disc or torus blocks our line of sight to a compact H II region where hydrogen lines arise. An equatorial disc geometry is favourable because it allows the escape of UV radiation in the polar direction, needed to ionize gas in the lobes. The dusty equatorial disc itself must be fairly compact compared with the rest of the nebula, since it does not cause severe extinction toward the northern polar lobe. Such a compact equatorial disc may conceivably have helped to pinch the waist of the expanding nebula (Frank 1999), but other explanations for the strong bipolarity exist as well (Balick & Frank 2002).

6.2 Nuclear density

Some of the bright emission lines in Fig. 2(b) and Table 5 are not actually emitted by the nucleus, but instead come from gas in the polar lobes included in the slit aperture at the somewhat inadequate spatial resolution used here. Inspection of the 2D long-slit spectra and also Fig. 6 indicate that some good examples of this trend are [O II] λλ3766, 3729, [S II] λλ6717, 6731, and [N II] λ6583, which show that emission directly from the bright nucleus is either very weak or absent. Unfortunately, these lines offer convenient density

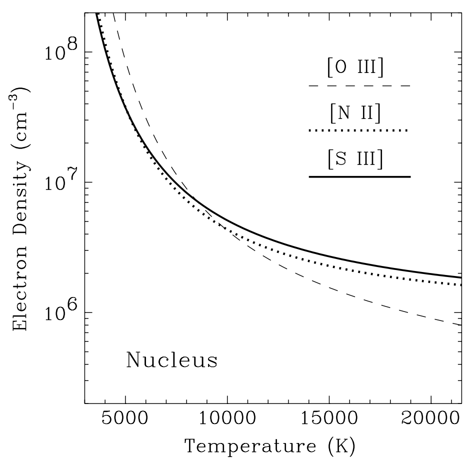

Figure 12. Same as in Fig. 9 but for the bright nucleus; curves for electron density as a function of temperature corresponding to the dereddened line ratios of [O III], [N II] and [S III]. Corrections have been applied to the intensities in Table 5 to account for contamination from circumstellar gas in the polar lobes along the line of sight to the bright nucleus.

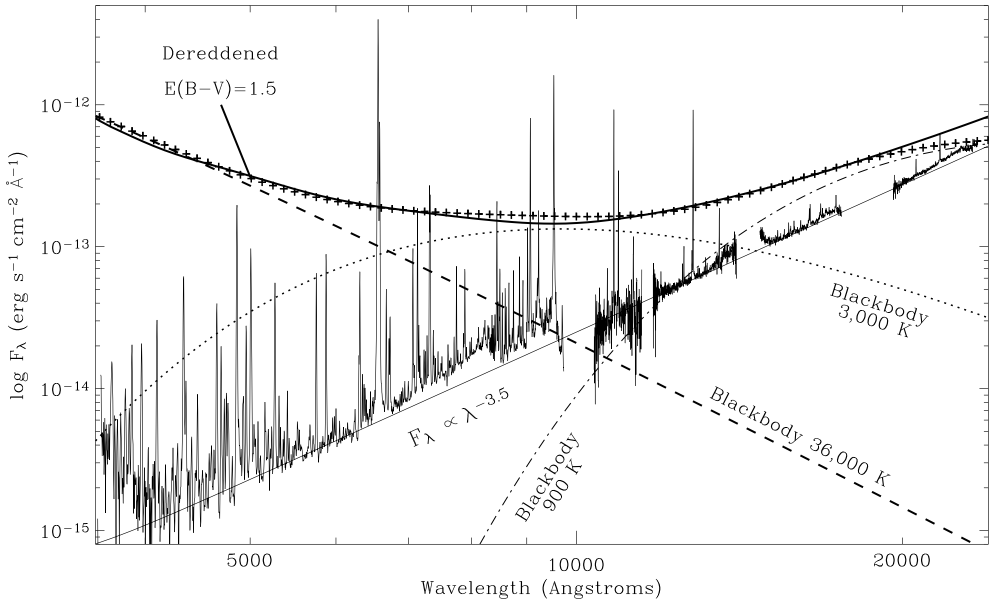

Figure 13. Complete 3600–23 000 Å spectrum of the bright nucleus of Mz 3 on a log–log plot. The observed continuum is approximated by a power law with $F_\lambda \propto \lambda^{3.5}$. The thick solid line shows this power-law continuum dereddened with $E(B - V) = 1.5$ derived from hydrogen lines in the nucleus. Small crosses show the total of three separate blackbody components at 36 000 K (dashed), 3000 K (dotted) and 900 K (dot-dashed).

diagnostics in nebular gas, but their weakness only gives lower limits in the nucleus of Mz 3.

The absence of these lines is caused by collisional de-excitation at high density, rather than depletion of these ions due to higher ionization. For example, while [O II] λλ3766, 3729 and [N II] λ6583 are very weak in the nucleus, lines of O I and [N I] are indeed seen there. Furthermore, lines of the same ionization state that are transitions from higher levels with higher critical densities are clearly seen in the nucleus, such as [O II] λ7325 and [N II] λ5755 (see Fig. 6). Thus, if the critical densities are known, the absence of certain lines in the nucleus can be used to infer the characteristic electron density there if it is assumed that their upper levels are depopulated by collisional de-excitation. Guided by various lines that appear to be quenched, and the presence of several lines that are not, the electron density in the ionized portion of the nucleus must be well above 10^5 cm^{-3}. [O III] λλ4959, 5007 and [S III] λλ9069, 9532 have higher critical densities and are detected in the nucleus, but Fig. 6 indicates that the intensities in Table 5 need to be adjusted somewhat because of contamination by emission from the polar lobes. If such corrections are applied, the usual [O III] and [S III] ratios (and the [N II] line ratios) indicate electron densities in the nucleus near 6×10^6 cm^{-3} for electron temperatures between 8000 and 10 000 K, as indicated by Fig. 12. Electron densities in the nucleus of Mz 3 exceed 10^6 cm^{-3} and even approach 10^7 cm^{-3} for reasonable electron temperatures. Zhang & Liu (2002) derive a similar density from [Fe III] lines in the nucleus.

6.3 Continuum emission

Figs 2 and 3 reveal very red continuum emission from the nucleus. It is barely detected at the shortest optical wavelengths, and is very strong in the IR. Images in Fig. 1 show a much brighter nucleus compared with the nebula than optical images (Redman et al. 2000).

Flux-calibrated spectra of the nucleus between 3600 and 23 000 Å are shown on a log–log plot in Fig. 13, where the observed continuum level comes close to fitting a simple power-law spectrum with $F_\lambda \propto \lambda^{3.5}$. The most significant deviations from this simple power-law continuum are in the Balmer and Paschen continua, and some excess emission is perceptible in the Brackett and Pfund continua as well.

Fig. 13 also shows this simple power law dereddened by the value of $E(B - V) = 1.5$ indicated by hydrogen lines in the nucleus (Fig. 11); this dereddened continuum may give essential clues to the nature of Mz 3. The dereddened continuum level at the shortest wavelengths requires the presence of a hot star in the system, approximated by a 36 000-K blackbody shown by the dashed line in Fig. 13.[5] The remaining dereddened continuum flux requires additional emission components; a possible fit is shown with small crosses in Fig. 13, produced by combining the hot blackbody with a Planck function at 3000 K and a blackbody at 900 K with a λ^{-1} emissivity law suitable for optically thin dust emission. The 900-K dust component depends on assumed grain parameters, and probably represents hot dust at a range of temperatures. The model slightly overestimates the dereddened power law near 9000 Å, but this is good because the simple power law underestimates the actual observed continuum flux at the same wavelength.[6] The dereddened continuum cannot be reproduced using only a hot star and dust, since dust is likely to melt at temperatures above 1500 K. Thus, the 3000-K blackbody may reveal the presence of both a late-type giant and a hot star in the nucleus Mz 3 – this would seem to indicate that Mz 3 may indeed be a symbiotic binary system.

However, this is not necessarily a unique interpretation of the observed continuum flux. A hot star with strong free–free emission from a wind at near-IR wavelengths, combined with circumstellar

[5] This temperature is chosen because of the result derived in Section 4.3, but almost any temperature blackbody above 25 000 K would be adequate to fit the continuum shape at blue wavelengths.

[6] The remaining discrepancy between the dereddened continuum and the model at the longest wavelengths in Fig. 13 can easily be rectified by adding an additional cool dust component, which is required to fit the mid-IR fluxes from the nucleus anyway (see Aitken & Roche 1982; Quinn et al. 1996).

dust, might also account for the continuum emission, but this is harder to model in a simple way. The massive star η Carinae is a highly reddened hot star with powerful free–free wind emission and hot circumstellar dust, and it shows a steep nearly power-law continuum at optical and near-IR wavelengths (Rodgers & Searle 1967). η Carinae gives an extreme example of how a rotating star with severe mass loss might produce a bipolar nebula with apparent structure similar to Mz 3, although there is not a yet a reason to favour such an interpretation over a symbiotic binary model for Mz 3.

In any case, a hot ∼36 000 K continuum source is needed to account for the blue continuum emission. The dereddened flux of the hot component in Fig. 13 at a wavelength of ∼5500 Å is $F_\lambda \approx 2 \times 10^{-13}$ erg s^{-1} cm^{-2} Å^{-1}, or $m_V \approx 10.5$. With a bolometric correction of approximately −3.63 mag for a 36 000 K star, the observed optical continuum would be consistent with the 10 000 $L_\odot$ source inferred in Section 4.3 if its distance were ∼2.6 kpc. This may be just an upper bound to the distance, since the observed optical continuum might not trace the true luminosity of the central engine; for instance, the photosphere of the hot star might suffer more extinction than hydrogen lines in the core, or the central star may appear underluminous if it is surrounded by an accretion disc. Regardless, this distance is close to the value of ∼2.7 kpc found by Kingsburgh & English (1992).

6.4 The evolutionary state of the hot star

With $T = 36\,000$ K and $L = 10\,000$ $L_\odot$, the hot component in the nucleus of Mz 3 sits comfortably on a typical post-AGB evolutionary track for an intermediate-mass progenitor star. At this position, it is likely that the star has just recently left the AGB, perhaps in the last 10 000–20 000 years. Thus, the post-AGB age is not much longer than a probable dynamical age for the nebula of $t = R/v$ (∼10^3 yr). While the material in and near the bright nucleus is most likely donated by the wind of the cool companion star, it is interesting to speculate that some of the material in or surrounding the bipolar nebula (especially some 'outer debris') may be stellar ejecta from former outer layers of the hot post-AGB star.

7 DISCUSSION

7.1 Comparison with M 2-9

Mz 3 is sometimes compared with M 2-9, the 'Butterfly Nebula' (Lopez & Meaburn 1983; Balick 1989), and this comparison is further justified by the data presented above. The most striking similarity is perhaps their observed morphology in images: both objects are narrow-waisted bipolar nebulae with bright point-like nuclei. Their spatially dependent spectra are remarkably similar as well. With Fig. 2 in-hand, one could read the description and analysis of the optical spectrum of M 2-9 by Allen & Swings (1972) and mistake it for an accurate description of Mz 3. Some of the most striking characteristics are common to both objects, such as the prominent [Fe III] lines, the large range of ionization, and the high nuclear densities between 10^6 and 10^7 cm^{-3}. Also, the detailed variation of some observed line ratios across the major axis of both nebulae are quite similar (compare Figs 6 and 7 with observations of M 2-9 by Phillips & Cuesta 1999). Finally, the highly reddened optical to near-IR continuum of Mz 3 comes close to a simple power law with $F_\lambda \propto \lambda^{3.5}$ (Fig. 13), similar to the observed continuum of M 2-9 (Swings & Andrillat 1979; Hora & Latter 1994). Both objects have strong thermal-IR excess due to warm dust (Aitken & Roche 1982; Quinn et al. 1996). Balick (1989) and Allen & Swings (1972) have compared the nuclear spectrum of M 2-9 with that of η Car, B[e] stars, galactic nuclei, and symbiotic stars such as RR Tel; the same comparisons apply to Mz 3. Because of all these similarities, it is quite likely that Mz 3 and M 2-9 share a similar evolutionary history, which may be different from other bipolar planetary nebulae, and more similar to those of eruptions of symbiotic stars (Balick 1989; Corradi & Schwarz 1993)

Because of these remarkable similarities, differences between the two objects are all the more noteworthy. Perhaps the most striking difference between spectra of the two objects arises in the near-IR: *there is no trace of molecular hydrogen emission in Mz 3*, while near-IR lines of H_2 are quite prominent in M 2-9. In images and spatially resolved near-IR spectra (Hora & Latter 1994), M 2-9 has an outer layer in its bipolar lobes (much like η Carinae; Smith 2002) where the H_2 1–0 S(1) line at 2.122 μm is as much as 20 times stronger than Brγ. Even at its weakest position in an ionized knot inside a polar lobe of M 2-9, the H_2 2.122 μm/Brγ intensity ratio is 0.15. In Mz 3, however, this line of molecular hydrogen is not detected anywhere across the nebula, and observational limits to its observed flux suggest that the H_2 2.122 μm/Brγ intensity ratio is less than 0.003, which implies that in Mz 3, lines of molecular hydrogen are 50–5000 times weaker than in M 2-9. Some molecular hydrogen may exist in the outer parts of the polar lobes or in shielded equatorial zones of Mz 3, and deeper K-band spectroscopy of positional offsets would be worthwhile. Nevertheless, the difference between Mz 3 and M 2-9 is dramatic, and it may be an important clue to the mass-loss mechanism that formed each nebula. The lack of H_2 in Mz 3 is also surprising, since Kastner et al. (1996) found a strong correlation between such H_2 emission and bipolar structure in planetary nebulae. Other differences exist as well, such as details of the observed morphology – the polar lobes of Mz 3 are more mottled and rounded (seemingly more prone to hydrodynamic instabilities), and those of M 2-9 are more smooth and open-ended along the polar axis. Mz 3 is not yet known to show the same temporal variability in the polar lobes as M 2-9 (Doyle et al. 2000).

7.2 A compact disc in the nucleus?

What is the nature of the high-density nucleus of Mz 3? Several observations of Mz 3 are consistent with the presence of a circumstellar (or circumbinary) disc in the system, and a few observations presented in this paper suggest quite strongly that some emission from the bright nucleus does in fact arise in a compact equatorial disc geometry.

(i) *Extinction.* Reddening of the nuclear spectrum suggests more than a magnitude of extra line-of-sight extinction than toward the polar lobes, and Fig. 7(d) also suggests a localized dramatic increase in the extinction toward the nucleus of Mz 3. Since the observed nebular morphology of Mz 3 indicates that it is observed at high inclination, our line of sight could intercept a flared dusty equatorial disc.

(ii) *Range of ionization.* The nuclear spectrum shows a wide range of ionization, from O I and [Fe II], residing in regions where hydrogen is neutral, up to He I and [O III]. This suggests that the high-density nucleus is radiation-bounded, lacking sufficient Lyman continuum to photoionize all the gas. However, high-ionization [O III] and He I zones are seen at large distances from the star in the polar lobes (see Fig. 1). The necessary far-UV flux could not escape the very dense $n_e \sim 10^6$–10^7 cm^{-3} nucleus if it were spherically symmetric (even if the high densities were in knots 100 times more dense than their surroundings), but the UV radiation could escape in the polar directions if the dense material resides in an equatorial disc.

If a disc causes a non-isotropic ionization field by blocking far-UV radiation at low latitudes, it may explain the apparent latitude dependence of excitation shown in Figs 1(d) and (f), where the side walls of the bipolar lobes have lower excitation than material in the caps of the lobes near the polar axis (where bright He I emission is seen). A compact circumstellar disc in the nucleus also has obvious applications for explaining the strong bipolar morphology of the nebula of Mz 3, by perhaps constricting the outflow near the equator. A compact disc could arise either from equatorial excretion by a rapidly rotating star, or perhaps in a symbiotic binary system where the wind and ionization of a hot star dominates and then confines a slower denser wind to low latitudes, creating a dense equatorial H II region.

Future observations can help constrain the nature of the disc, which may lead to an estimate of the current mass-loss rate of the system. For example, high dispersion line profiles of [N II] lines in the nucleus (Lopez & Meaburn 1983) are similar to narrow emission lines in RY Scuti, where the emission is known to arise in an ionized circumstellar disc/torus (Smith et al. 2002). More detailed observations of line profiles in Mz 3 over a wide range of ionization could constrain the geometry; O I and [O III] line profiles should be different for a thin disc compared with a scenario where a spherically symmetric red giant wind is ionized by a hot companion star, for instance. Also, if some lines in the nucleus arise in such a dense ionized wind in a binary system, orbital reflex motion should be detectable if the lines are monitored over time, since our view of Mz 3 is close to the equator. No temporal variability has yet been reported for Mz 3. Finally, the best way to constrain the geometry of the core may be with higher-resolution images and spectra taken with *HST*.

ACKNOWLEDGMENTS

I am grateful to Bruce Balick for interesting discussions concerning other observations of Mz 3, to Gary Ferland for helping to get me started with using CLOUDY, and to an anonymous referee. NOAO and the Graduate School of the University of Minnesota each covered part of my travel expenses to Chile and accommodation while at CTIO. As usual, members of the CTIO staff were very hospitable and I benefited from their assistance while obtaining the observations. This research was supported in part by NASA grant NAG-12279 to the University of Colorado.

REFERENCES

Aitken D.K., Roche P.F., 1982, MNRAS, 200, 217
Allen D.A., Swings J.P., 1972, ApJ, 174, 583
Balick B., 1989, AJ, 97, 476
Balick B., 2000, in ASP Conf. Ser. Vol. 199, Asymmetrical Planetary Nebulae II: from Origins to Microstructures. Astron. Soc. Pac., San Francisco, p. 41
Balick B., Frank A., 2002, ARA&A, 40, 439
Calvet N., Peimbert M., 1983, Rev. Mex. Astron. Astrofis., 5, 319
Cardelli J.A., Clayton G.C., Mathis J.S., 1989, ApJ, 345, 245
Cohen M., Fitzgerald M.P., Kunkel W., Lasker B.M., Osmer P.S., 1978, ApJ, 221, 151
Corradi R.L.M., 2000, in ASP Conf. Ser. Vol. 199, Asymmetrical Planetary Nebulae II: From Origins to Microstructures. Astron. Soc. Pac., San Francisco, p. 25
Corradi R.L.M., Schwarz H.E., 1993, A&A, 268, 714
Corradi R.L.M., Livio M., Schwarz H.E., Munari U., 2000, in ASP Conf. Ser. Vol. 199, Asymmetrical Planetary Nebulae II: From Origins to Microstructures. Astron. Soc. Pac., San Francisco, p. 175
Doyle S., Balick B., Corradi R.L.M., Schwarz H.E., 2000, AJ, 119, 1339
Evans D.A., Thackeray A.D., 1950, MNRAS, 110, 429
Evans D.S., 1959, MNRAS, 119, 150
Ferland G.J., 1996, Hazy, a brief introduction to CLOUDY, Univ. Kentucky Department of Physics and Astronomy Internal Report
Frank A., 1999, New Astron. Rev., 43, 31
Graham J.R., Wright G.S., Longmore A.J., 1987, ApJ, 313, 847
Henry R.C.B., Kwitter K.B., Buell J., 1998, Rev. Mex. Astron. Astrofis., Ser. Conf., 7, 30
Hora J.L., Latter W.B., 1994, ApJ, 437, 281
Hummer D.G., Storey P.J., 1987, MNRAS, 224, 801
Kastner J.H., Weintraub D.A., Gatley I., Merrill K.M., Probst R.G., 1996, ApJ, 462, 777
Kingsburgh R.L., English J., 1992, MNRAS, 259, 635
Kwitter K.B., Henry R.B.C., 2000, in ASP Conf. Ser. Vol. 199, Asymmetrical Planetary Nebulae II: From Origins to Microstructures. Astron. Soc. Pac., San Francisco, p. 329
Kwitter K.B., Henry R.B.C., Milingo J.B., 2003, PASP, 115, 80
Liu X.W. et al., 2001, MNRAS, 323, 343
Lopez J.A., Meaburn J., 1983, MNRAS, 204, 203
Meaburn J., Walsh J.R., 1985, MNRAS, 215, 761
Menzel D.H., 1922, Harvard Bull., 777
Merrill P.W., 1928, ApJ, 67, 179
Minkowski R., 1947, PASP, 59, 237
Nussbaumer H., Storey P.J., 1988, A&A, 193, 327
Osterbrock D.E., 1989, Astrophysics of Gaseous Nebulae and Active Galactic Nuclei. Univ. Science Books, Mill Valley
Phillips J.P., Cuesta L., 1999, AJ, 118, 2919
Redman M.P., O'Connor J.A., Holloway A.J., Bruce M., Meaburn J., 2000, MNRAS, 312, L23
Rodgers A.W., Searle L., 1967, MNRAS, 135, 99
Scarrott S.M., Scarrott R.M.J., 1995, MNRAS, 277, 277
Schmeja S., Mineswenger S., 2001, A&A, 377, L18
Smith N., 2002, MNRAS, 337, 1252
Smith N., Gehrz R.D., Stahl O., Balick B., Kaufer A., 2002, ApJ, 578, 464
Swings J.P., Andrillat Y., 1979, A&A, 74, 85
Quinn D.E., Moore T.J.T., Smith R.G., Smith C.H., Fujiyoshi T., 1996, MNRAS, 283, 1379
Zhang Y., Liu X.W., 2002, MNRAS, 337, 499

This paper has been typeset from a TEX/LATEX file prepared by the author.